circulation Γ at the origin is given by

$$\varphi_m = \frac{\Gamma s}{2\pi}\frac{\sin\theta}{r} + \frac{\Gamma s}{2\pi}\frac{\sin\theta}{r}\frac{x}{(x^2+\beta^2r^2)^{1/2}} = \varphi_{m_1}(r,\theta) + \varphi_{m_2}(x,r,\theta) \quad (9)$$

Since the disturbance potential consists of two terms, one independent of x and the other dependent of x, the interference potential may be split into two parts as

$$\varphi_i = \varphi_{i_1}(r,\theta) + \varphi_{i_2}(x,r,\theta) \quad (10)$$

The potential φ_{i_1}, induced by φ_{m_1}, is found as

$$\varphi_{i_1} = \frac{\Gamma s}{2\pi b}\sum_{m=1,3,5}^{\infty} D_m r^m \sin m\theta \quad (11)$$

The transformed potential $\tilde{\varphi}_{i_2}$, due to φ_{m_2}, is reduced from Eq. (4) to

$$\tilde{\varphi}_{i_2} = \sum_{m=1,3,5}^{\infty}(G_m + iE_m)\sin m\theta I_m\left(\frac{qr}{b}\right) \quad (12)$$

The coefficients D_m, G_m, and E_m are determined from matching the boundary conditions at discrete points by the point-matching method.

The interference potential is obtained from Eqs. (11) and (12)

$$\varphi_i(x,r,\theta) = \frac{\Gamma s}{2\pi b}\left\{\sum_{m=1,3,5}^{\infty} D_m r^m \sin m\theta + \frac{2}{\pi}\int_0^{\infty}\sum_{m=1,3,5}^{\infty}\sin(m\theta)I_m\left(\frac{qr}{b}\right)\left[G_m\cos\left(\frac{qx}{\beta b}\right) + E_m\sin\left(\frac{qx}{\beta b}\right)\right]dq\right\} \quad (13)$$

The lift interference factor δ and the streamline curvature δ_1 are defined as

$$\delta = \frac{C}{SC_L}\frac{1}{U}\frac{\partial\varphi_i}{\partial z} \text{ and } \delta_1 = \frac{2\beta h}{S}\frac{C}{C_L}\frac{1}{U}\left(\frac{\partial^2\varphi_i}{\partial x\,\partial z}\right)_{r=0}$$

respectively.

The lift interference factor and its distribution along the centerline are shown in Figs. 1 and 2 for test sections of various height-to-width ratios and different porosities. Figure 3 shows the streamline curvature at the model position.

All numerical results presented herein were determined by using ten terms of the infinite series and twenty points along one quadrant of the boundary because of the symmetrical property of this problem. In order to examine the accuracy of the present method, the case of closed vertical walls and perforated horizontal walls has been calculated and compared with the results obtained in a closed form by another method in Ref. 8. The comparison indicates excellent agreement for the case of a square or nearly square tunnel and satisfactory agreement for the case of test sections having height-to-width ratios around 0.5. Similar results have been noted for a slotted wall tunnel as previously reported in Ref. 5.

It is interesting to note that zero interference can be obtained by the proper combination of porosity in the horizontal and vertical walls. The proper combination of porosity required for zero lift interference is shown in Fig. 4 and indicates the lift interference is insensitive to the porosity of the vertical walls for height-to-width ratios less than 0.8, as is also the case for the slotted wall tunnel.[5]

References

[1] Pindzola, M. and Chew, W. L., "A Summary of Perforated Wall Wind Tunnel Studies at the Arnold Engineering Development Center," TR-60-9, Aug. 1960, Arnold Engineering Development Center.

[2] Treon, S. L. et al., "Data Correlation from Investigation of a High-Subsonic Speed Transport Aircraft Model in Three Major Transonic Wind Tunnels," AIAA Paper 69-794, Los Angeles, Calif., 1969.

[3] Garner, H. C. et al., "Subsonic Wind Tunnel Wall Corrections," AGARDograph 109, Oct. 1966.

[4] Rushton, K. R. and Laing, L. M., "A General Method of Studying Steady Lift Interference in Slotted and Perforated Tunnels," R and M 3567, 1968, Aeronautical Research Council.

[5] Lo, C. F. and Binion, T. W., Jr., "A V/STOL Wind Tunnel Wall Interference Study," AIAA Paper 69-171, New York, 1969; also *Journal of Aircraft*, Vol. 7, No. 1, Jan.-Feb. 1970, pp. 51–57.

[6] Lo, C. F. and Oliver, R. H. "Boundary Interference in a Rectangular Wind Tunnel Wire Perforated Walls,"TR-70-67, April 1970, Arnold Engineering Development Center.

[7] Goodman, T. R., "The Porous Wall Wind Tunnel, Part II. Interference Effect on a Cylindrical Body in a Two-Dimensional Tunnel at Subsonic Speed," Rept. AD-594-A-3, 1950, Cornell Aeronautical Lab. Inc.

[8] Oliver, R. H., "Determination of Blockage and Lift Interference for Rectangular Wind Tunnels with Perforated Walls," MS thesis, Aug. 1969, University of Tennessee, Knoxville, Tenn.

Simplified Analysis of a Trifragment Rotor Disk Interaction with a Containment Ring

R. Bruce McCallum*

Massachusetts Institute of Technology, Cambridge, Mass.

Introduction

RECENT spin-pit tests have been performed at the Naval Air Propulsion Test Center, Philadelphia, Pa. on 15-in.-i.d. steel rings of various thicknesses using comparatively nondeforming steel fragments (as illustrated in Fig. 2) to evaluate the possibility of using an inexpensive standard fragment generator in future parametric studies. The purpose of these parametric studies would be to test the merits of various materials to be used for jet engine burst rotor containment devices. In those tests where containment-ring failure occurred, high-speed photographs show a "shattering" effect, where the ring appears to separate in one or more locations with little noticeable deformation, within 400 μsec after collision. Since other tests, using bladed rotor segments as fragments, show considerable ring deformation before ring failure occurs, the use of nondeforming fragments has been considered by some as an unsatisfactory substitute for the more expensive bladed-rotor fragments.

In the present Note, the results of an analysis (using a computer program written at Massachusetts Institute of

Received January 29, 1970. This research is supported by Grant No. NGR 22-009-339 from the Aerospace Safety Research and Data Institute, Lewis Research Center, NASA, Cleveland, Ohio. The author is indebted to A. A. Martino and G. J. Mangano of Naval Air Propulsion Test Center., Philadelphia for their experimental data, and he gratefully acknowledges the comments and advice given to him by E. A. Witmer and J. W. Leech of Aeroelastic and Structures Research Laboratory, Massachusetts Institute of Technology. The computations were carried out at the Massachusetts Institute of Technology Information Processing Center.

* Senior Research Engineer, Aeroelastic and Structures Research Laboratory.

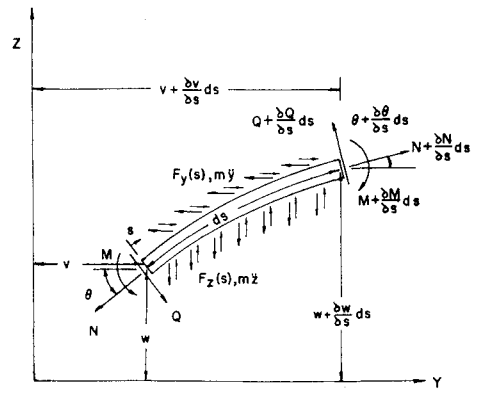

Fig. 1 Schematic of structural element.

Technology (M.I.T. called JET 1) are presented which indicate that the observed phenomenon is caused by a shearing of the ring at the point of initial fragment collision.

JET 1 Program

The JET 1 program uses a finite-difference formulation of the partial differential equations of dynamic equilibrium to predict the elastic-plastic large deflection transient response of a ring structure. Figure 1 shows an element of a ring in its instantaneous large-deformation state. The internal forces acting on this element are the axial force N, the transverse shear force Q, and the bending moment M. The external forces $F_y(s)$ and $F_z(s)$ and the inertial forces $m\ddot{y}$ and $m\ddot{z}$ caused by accelerations, are also shown.

From force equilibrium, one obtains

$$(\partial/\partial s)(N\cos\Theta) - (\partial/\partial s)(Q\sin\Theta) + F_y - m\ddot{v} = 0 \quad (1)$$

$$(\partial/\partial s)(N\sin\Theta) + (\partial/\partial s)(Q\cos\Theta) + F_z - m\ddot{w} = 0 \quad (2)$$

and from equilibrium of moments

$$(\partial M/\partial s) - Q = 0 \quad (3)$$

where s and Θ are defined in Fig. 1.

When these equations are finite-differenced in space, they become equivalent to a lumped mass model with interconnecting straight, massless, extensible bars with bending occurring only at each mass point. The normal force and bending moment at each station are evaluated by summing forces and moments of each of several assumed layers through the ring thickness. The central three-point difference approximation is then used to evaluate the second time

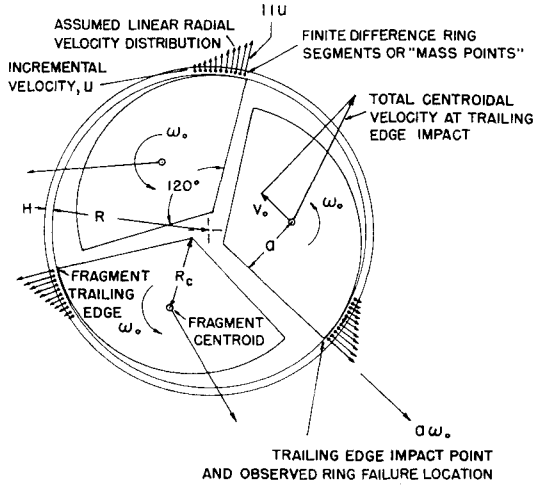

Fig. 2 Schematic of containment ring and three rotor disk fragments at instant of trailing-edge impact, with assumed initial linear velocity distribution.

Table 1 Test parameters

Parameter	Test 1 (NAPTC 64)	Test 2 (NAPTC 70)
Ring radius R, in.	7.438	7.501
Ring thickness H, in.	0.375	0.341
Ring length B, in.	1.502	1.501
Rotor disk radius, in.	7.00	7.00
Fragment centroidal radius R_c, in.	3.86	3.86
Fragment mass M_f, lb-sec/in.	0.0136	0.0136
Fragment moment of inertia about its centroid I_f, lb-sec-in.	0.135	0.135
Rotor disk rotational velocity at release ω_0, rad/sec	950	596
Ring material, steel	4130	4130
Fragment trailing edge velocity at impact $V_0 + a\omega_0$, in/sec	1900	840

derivatives of v and w. Although not discussed here (see Refs. 1 and 2 for a complete description and Ref. 3 for related information) material strain-hardening and strain-rate effects are included in the JET 1 program.

Test Parameters

The JET 1 program was used to analyze two similar Naval Air Propulsion Test Center (NAPTC) spin-pit tests incorporating nondeforming 4130 steel fragments. In the first test, the ring failed in the manner described previously; in the second test, the ring remained intact. The pertinent dimensions for each test are presented in Table 1.

Observations From High-Speed Photographs

High-speed photographs, initiated by fragment contact with the ring, were taken of both events. In the first test, the interval between photographs was 67.4 μsec and a failure in the ring was evident by the sixth frame. When the failure point on the ring was located on the initial frame in the series, the impact point of one of the fragment's trailing edge was seen to coincide with the failure point. Since the fragment trailing edge is essentially a right angle, suspicions were aroused that a shear failure, caused by the sharp-edged impulsive-type load supplied by the fragment impact, had occurred.

Analysis Parameters

The quasi-static stress-strain curve for the 4130 steel used to manufacture both rings was obtained by a tensile test performed by NAPTC personnel. A piece-wise linear stress-strain curve that approximated the given curve was then formed with the following stress strain coordinates (σ, ϵ): (0 psi, 0 in./in.); (0.10×10^6, 0.33×10^{-2}); (0.115×10^6, 0.582×10^{-2}); (0.125×10^6, 0.92×10^{-1}). The static value of ultimate shear stress σ_{sult} for 4130 steel was obtained from Ref. 4 as 82,000 psi.

For both rings studied, a total number of 192 masses was used in the analysis to obtain satisfactory convergence for the value of shear stress Q/BH in each ring.

Next, the forcing function acting on each ring caused by its interaction with each fragment had to be described. Ideally, this would be a known time-dependent force distribution applied to portions of the ring. These forces are not known a priori, however; therefore, an impulse loading was assumed by describing the initial velocity of the ring portions affected. From the measured burst RPM, and the physical shape of the fragment, the position and velocity of each fragment at trailing-edge impact was determined. Using velocity vector diagrams, a fragment trailing-edge velocity normal to the ring for each test was obtained. The much higher tangential velocity obtained was not considered in the analysis because the high-speed photographs showed

no appreciable angular acceleration of the ring in the initial phase of each test, an indication that the fragments readily slid along the inside surface. A triangular radial velocity distribution acting over three ring segments of eleven masses each was then assumed as shown in Fig. 2. This tentative distribution was chosen on the basis of the apparent contact area shown in the high-speed photographs.

In order to calculate an initial velocity value for the mass points, an elastic collision was assumed. Conservation of linear momentum, angular momentum, and kinetic energy before and after collision yields the following three equations with three unknowns:

$$M_f V_0 = M_f V_f + m \sum_{j=1}^{11} ju$$

$$I_f \omega_0 = I_f \omega_f + ma \sum_{j=1}^{11} ju \qquad (4)$$

$$\tfrac{1}{2} M_f V_0^2 + \tfrac{1}{2} I_f \omega_0^2 = \tfrac{1}{2} M_f V_f^2 + \tfrac{1}{2} I_f \omega_f^2 + \tfrac{1}{2} m \sum_{j=1}^{11} (ju)^2$$

where V = fragment centroidal velocity normal to the ring, the incremental velocity u and the quantity a are defined in Fig. 2; the subscripts o and f on V and ω indicate before and after collision, respectively. When these equations are solved simultaneously, the following equation for the incremental velocity u is obtained:

$$u = 132(V_0 + a\omega_0)/[4356(m/M_f + a^2 m/I_f) + 506] \qquad (5)$$

The resulting error in momentum incurred by choosing the imparted velocity direction to be radial at each mass point, rather than the single fragment direction, was neglected.

Results

The value of the predicted shear stress occurring at the point of impact vs time, obtained from the JET 1 analysis, is plotted in Fig. 3 for each of the two test cases. The maximum shear stress value obtained for the run in which the ring failed was 92,300 psi, which substantially exceeds the Ref. 4 value of the ultimate shear stress for 4130 steel. The maximum shear-stress value obtained for the run in which the ring did not fail was 65,220 psi, which was considerably below the ultimate shear-stress value.

Strain rate effects were not included in the analysis because data for 4130 steel at high strain rates were not available. Although this omission significantly affects the maximum value of shear stress obtained, the fact that the static value of ultimate shear stress was used to test for failure makes the analysis consistent.

From Fig. 3, the calculated time to failure for case 1 is seen to occur within 1 μsec after impact, whereas the ring failure is evident in the high-speed photographs only after approximately 400 μsec. Part of this rather large discrepancy can be explained by the fact that the gap in the ring when failure was first detected from the photographs is on the order of $\frac{1}{2}$ in., and since the initial ring mass-point velocity at the impact point is approximately 5000 in./sec, it will take over 100 μsec for a failure to be detectable for this reason alone.

Conclusions

The present initial results of this continuing study indicate that containment rings may be shear failure critical if certain types of fragments are used. In addition to the previously described nondeforming type of fragment, fragments of interest could include those from the large-diameter fan blades incorporated in the new generation high mass-flow jet engines to be used on "Jumbo Jet" type aircraft. When analyses are made similar to those described here, care must be exercised that enough mass increments are used to obtain convergent values of shear stress. Although applicable to other types of fragments in a general way, the aforementioned impulse calculation should obviously be used in its present form only for nondeforming fragments, since the energy used to deform bladed rotors will decrease, to some degree, the amount of energy transferred to the ring. Finally, the results indicate that perhaps a new nondeforming fragment, possibly with rounded edges, can be found which better simulates the types of ring response that have been obtained from bladed rotor interaction tests.

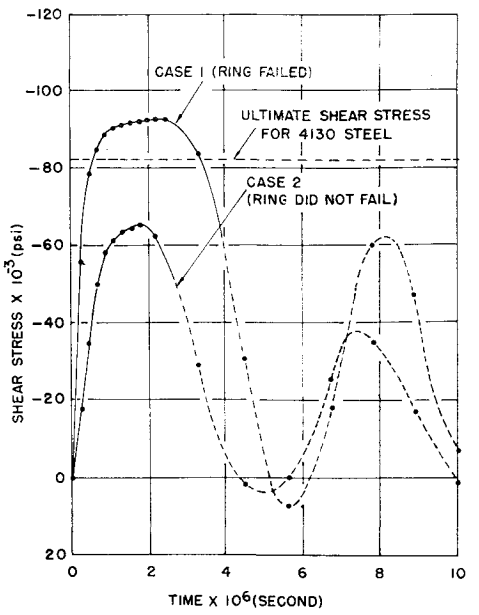

Fig. 3 Calculated shear stress at each impact point vs time.

References

[1] McCallum, R. B., Leech, J. W., and Witmer, E. A., "Progress in the Analysis of Jet Engine Burst-Rotor Containment Devices," ASRL TR 154-1, Aug. 1969, Aeroelastic and Structures Research Lab., Massachusetts Institute of Technology.

[2] Witmer, E. A. et al., "Large Dynamic Deformations of Beams, Rings, Plates, and Shells," *AIAA Journal*, Vol. 1, No. 8, Aug. 1963, pp. 1848–1857.

[3] Leech, J. W., Witmer, E. A., and Pian, T. H. H., "Numerical Calculation Technique for Large Elastic-Plastic Transient Deformations of Thin Shells," *AIAA Journal*, Vol. 6, No. 12, Dec. 1968, pp. 2352–2359.

[4] "Strenth of Metal Aircraft Elements," *Military Handbook*, MIL-HDBK-5, March 1959, Armed Forces Supply Support Center, Washington D.C.

Critical Preston-Tube Sizes

JERRY M. ALLEN*
NASA Langley Research Center, Hampton, Va.

Nomenclature†

C_f = local skin-friction coefficient
C_F = average skin-friction coefficient
d = Preston-tube diameter

Received October 30, 1969.

* Aerospace Engineer, Full-Scale Research Division. Member AIAA.

† Primed quantities are evaluated at reference temperature.